Powder Technology 327 (2018) 489–499

Contents lists available at ScienceDirect

Powder Technology

journal homepage: www.elsevier.com/locate/powtec

Controlled preparation of superparamagnetic Fe_3O_4@SiO_2@ZnO-Au core-shell photocatalyst with superior activity: RhB degradation and working mechanism

Dandan Wang [a,b,c,1], Donglai Han [d,1], Jinghai Yang [c,*], Jian Wang [c], Xiuyan Li [c,*], Hang Song [a]

[a] Changchun Institute of Optics, Fine Mechanics and Physics, Chinese Academy of Sciences, Changchun 130033, PR China
[b] University of Chinese Academy of Sciences, Beijing 100049, PR China
[c] Key Laboratory of Functional Materials Physics and Chemistry of the Ministry of Education, Jilin Normal University, Changchun 130103, PR China
[d] School of Materials Science and Engineering, Changchun University of Science and Technology, Changchun 130022, PR China

ARTICLE INFO

Article history:
Received 26 June 2017
Received in revised form 14 December 2017
Accepted 28 December 2017
Available online 10 January 2018

Keywords:
Magnetic separation
Core-shell structure
ZnO nanorods
Au nanoparticles
Photocatalysis

ABSTRACT

The designed synthesis of advanced ZnO heterostructures in a simple and mild way is of great significance, for the purpose of improving their photocatalytic performance and large-scale applications. Herein, a magnetic hierarchical microsphere Fe_3O_4@SiO_2@ZnO@Au (FSZA) was successfully synthesized by multistep chemical methods, in which magnetic Fe_3O_4@SiO_2 as core for the growth of ZnO nanorod-layer using microwave-assisted approach, followed by the functionalization of Au nanoparticles (NPs). Four FSZA microspheres (FSZA1, FSZA2, FSZA3, FSZA4) were controlled prepared by adjusting the concentration of the Au precursor for comparison. The as-prepared products were characterized SEM, TEM, XRD, VSM, N_2-sorption, photocurrent and XPS techniques. The results revealed that the as-synthesized microspheres have a good monodispersity, uniform core-shell structure and high magnetization. The photocatalytic test indicated the FSZA3 product possessed the best activity among all tested products, and the photodegradation rate of rhodamine B (RhB) reached 93.54% after UV irradiation of 80 min. The enhanced activity of FSZA3 was ascribed two major contributions, which were the larger specific surface area and the improved separation efficiency of the photogenerated carriers. The decomposition mechanism was discussed in detail. Additionally, such integrated FSZA3 photocatalyst was easily recovered by a magnet, which was reused at least five times without any appreciable reduction in photocatalytic efficiency.

1. Introduction

Water pollution due to the great industrial and population growth is one of the biggest challenges faced by human beings. To tackle this challenge, semiconductor-based photocatalysis has been consider as a "Green technology", in which the oxidation and reduction reactions are started by photoinduced generation of electron-hole pairs, followed by transfer of these charge carriers to the surface of photocatalysts, and then mineralize most of the organic contaminants into small inorganic molecules [1–3]. Remarkable research efforts have been focused on the fabrication of efficient semiconductor-based photocatalytic systems including TiO_2, ZnO, ZnSe [4–6]. In particular, ZnO as a n-type semiconductor with a wide-band gap of 3.2 eV, is one of the classiest and commonly used catalysts because of the low price, non-toxic nature, thermal stability, and high quantum efficiency [7,8].

But, the photocatalytic activity of ZnO materials still is limited by fast charge carrier recombination and low interfacial charge transfer rate [9]. Recently, rational design and fabrication of heterostructured ZnO nanomaterials have attracted increasing interest due to their potential of endowing the materials with excellent functions [10]. ZnO/metal heterostructures, particularly ZnO/Au heterostructures, have been paid more attention owing to their unique advanced electronic, optical, catalytic properties and high chemical stability [11,12]. In catalytic properties, on the one hand, Au NPs can facilitate electron excitation of ZnO semiconductor by creating local electrical field [13]. On the other hand, Au NPs and ZnO semiconductor would form Schottky barriers at their interfaces owing to their differences in work function and band alignment, leading to the obvious separation and transfer of photoexcited charges [14,15]. Therefore, the high-quality heterojunctions between Au NPs and ZnO semiconductor can significantly facilitate the effective charge transfer interfaces and reinforce the photocatalytic performance in applications. Furthermore, the photocatalytic activity of ZnO/Au heterostructure materials is strongly sensitive to the size of Au NPs [12,16]. Due to the fast rate of Au NPs formation, most of the common synthetic methods can't produce Au NPs with small and uniform size. The

* Corresponding authors.
E-mail addresses: jhyang1@jlnu.edu.cn (J. Yang), lixiuyan@jlnu.edu.cn (X. Li).
[1] The authors have the equal contribution to the manuscript.

https://doi.org/10.1016/j.powtec.2017.12.088
0032-5910/

aggregation will reduce the surface area and utilization ratio of Au NPs [17,18]. Thus, it is desirable to develop a facile method to prepare nanoscale, uniform, and well-disperse Au NPs on ZnO nanomaterials.

Alternatively, the separation of semiconductor-based photocatalysts from the treated water is a major bottleneck that restricts their large-scale applications. Although filtration, centrifuge, and immobilization of photocatalysts provide solutions for this draw-back, these additional steps are time-consuming and greatly increase cost of photocatalytic process [19,20]. To improve the practicability of semiconductor photocatalyst, magnetic materials such as Fe_3O_4 and γ-Fe_2O_3 have been extensively applied to fabricate magnetic multicomponent potocatalysts [8,21,22]. With the help of external magnetic force, magnetic materials provide a convenient approach for separating and manipulating photocatalysts, which makes solid-liquid phase separation fast, simple as well as highly effective. Accordingly, magnetic nanospheres, especially Fe_3O_4, have been widely studied in virtue of the outstanding combination of non-toxicity, flexible surface functionalization and sensitive magnetic response [22]. Meanwhile, SiO_2 coating technology has been studied to prevent Fe_3O_4 material from oxidation and fast heat transfer [23]. Yu et al. has reported that SiO_2 barrier layer can inhibit the migration of photoinduced carriers from the semiconductor photocatalyst to the magnetic core, which would reduce the photocatalytic activity [24].

In this work, a practical Fe_3O_4@SiO_2@ZnO@Au (FSZA) core-shell photocatalytic system was successfully constructed by multistep chemical methods, in which a facile approach was developed to prepare uniform and well-disperse Au NPs with a diameter of about 4 nm. Since the incorporation of the merits of multicomponent, including magnetic Fe_3O_4 core, SiO_2 barrier layer, ZnO nanorod-layer and moderate Au NPs, the FSZA3 core-shell heterostructure exhibited superior synergistic properties such as magnetic recovery and good photocatalytic properties in the process of RhB photodecomposition. Moreover, these properties are stable during five cycles. Accordingly, the decomposition mechanism of RhB over FSZA microspheres under UV irradiation was proposed.

2. Experimental

2.1. Materials

All the chemicals used in this experiment were of analytical grade and were used as received without further purification. Deionized water (resistivity > 18.0 MΩ cm) was used throughout the experiments.

2.2. Preparation of magnetic photocatalysts

The procedure for preparing FSZA core-shell microspheres is depicted in Scheme 1, which mainly consists of five steps. The specific synthesis processes for each growth step are illustrated as follows:

Step 1: Magnetic Fe_3O_4 (F) particles were prepared via solvothermal process [20]. Typically, $FeCl_3 \cdot 6H_2O$ (2.6 g) was dissolved in ethylene glycol (80 mL) under magnetic stirring to form a clear yellow solution. Subsequently, NaAc (4.0 g) was added to above solution and being stirred for 1 h. Then, trisodium citrate (1.0 g) was added by stirring. After the reactant was fully dissolved, the obtained homogeneous dispersion was transferred to a 100 mL Teflon-lined stainless-steel autoclave and heated at 200 °C for 10 h. The black powders were rinsed with deionized water and ethanol for five times. The product was then collected with the help of a magnet and dried in vacuum at 60 °C for 6 h.

Step 2: The SiO_2 interlayer was coated on the surface of F core by a modified Stöber method as described previously [25]. Briefly, the obtained F particles (0.5 g) were dispersed in a mixed solution, including deionized water (50 mL), ethanol (150 mL) and ammonia aqueous solution (25 wt%, 2.0 mL). After ultrasonication for 1 h, tetraethyl orthosilicate (0.8 mL) was added dropwise to above dispersion by stirring for another 2 h. Subsequently, the Fe_3O_4@SiO_2 (FS) product was collected and washed with deionized water for three times, and then dried under vacuum at 60 °C for further use.

Step 3: ZnO seeds were loaded on the surface of FS samples according to a previous report [26]. The as-prepared FS product (1.2 g) and $ZnAc_2 \cdot 2H_2O$ (0.36 g) were added to ethanol (54 mL) under ultrasound. Then, a mixture of ethanol (86 mL) and NaOH (0.2 g) was added dropwise to above solution. Subsequently, the obtained reaction system was maintained at 60 °C with mechanical stirring for 30 min. After washing with deionized water and ethanol for four times, the Fe_3O_4@SiO_2@ZnO-seeds (FSz) product was collected with an applied magnet field and then dried at 60 °C for following ZnO nanorods growth.

Step 4: ZnO nanorods grown on the surface of FSz product using microwave method. The FSz sample (0.4 g), $Zn(NO_3)_2 \cdot 6H_2O$ (2.7 g) and polyvinylpyrrolidone (2.7 g) were added to deionized water (200 mL). After mechanically stirring for 30 min, hexamethylenetetramine (1.3 g) and ethylene glycol (200 mL) were successively added to the above mixture under mechanically stirring. Subsequently, this solution was heated in a microwave oven for 15 min at a power setting of 550 W. The Fe_3O_4@SiO_2@ZnO (FSZ) product was washed with

Scheme 1. Schematic diagram for fabrication process of the FSZA core-shell photocatalyst.

deionized water for several times, collected with the help of a magnet, and dried in vacuum at 60 °C for 6 h.

Step 5: The deposition of Au NPs onto FSZ product was performed as follows. The obtained FST sample (0.5 g) was immersed in $HAuCl_4 \cdot 4H_2O$ solution (34 wt%). After mechanically stirring for 12 h, pouring the supernatant and collecting solid powder with the help of magnetic field. Then, the collected solid powder was dispersed in $NaBH_4$ aqueous solution (15 wt%, 500 mL). After being stirring for 10 min, the FSZA product was separated, repeatedly washed with deionized water, and dried at 60 °C. In this work, various amounts of $HAuCl_4 \cdot 3H_2O$ solution (5, 15, 25 and 35 mL) were employed to synthetize four FSZA products with different Au NPs contents. The obtained FSZA products were denoted as FSZA1, FSZA2, FSZA3 and FSZA4, respectively.

2.3. Characterization

The morphologies and microstructures of all as-obtained samples were observed by a field emission scanning electron microscopy (FESEM, JEOL 7800F) and a transmission electron microscopy (TEM, FEI Tenai G^2 F20). The X-ray diffraction (XRD) patterns of as-prepared samples were performed by a D/max-2500 copper rotating-anode X-ray powder diffraction with Cu-Kα radiation of wavelength $\lambda = 1.5406$ Å (40 kV, 200 mA). The magnetic properties of the obtained samples were assessed by using a vibrating sample magnetometer (VSM, Lake Shore 7407) at room temperature. N_2 adsorption isotherms and the Brunauer-Emmett-Teller (BET) surface areas of the as-prepared samples were measured by using a Nova l000 analyzer. The chemical compositions and valance bands of the synthesized samples were identified by a Thermo Scientific ESCALAB 250Xi A1440 system.

2.4. Photocurrent measurements

The photocurrent measurements were carried out by using a computer-controlled electrochemical work station (CHI-660C Instruments, China). Firstly, sample powder (10 mg) was dispersed into ethanol (0.5 mL) under sonication for 10 min to get slurry. The as-prepared slurry spread onto the conductive surface of clean indium tin oxide (ITO) glasses to form a photocatalyst film. The uncoated parts of ITO glass were isolated with epoxy resin. Subsequently, a standard three-electrode cell was used, which composed by the as-prepared samples coated on the indium tin oxide glass (1.0 cm × 4.0 cm) as the working electrode, a saturated calomel electrode (SCE) as a reference, and a platinum minigrid as a counter electrode. Then, the working electrode was immersed in a Na_2SO_4 electrolyte solution (0.5 M) and irradiated by a 300 W xenon lamp. The light/dark short circuit photocurrent response was recorded at an applied potential of + 1.0 V.

2.5. Photocatalytic activity measurement

The photocatalytic performances of the as-prepared samples were evaluated by the decomposition of RhB aqueous solution. A Xe lamp with a light intensity of 5 $W \cdot cm^{-2}$ (CEL-HXUV300 300 W) was used as the light source. Prior to irradiation, the RhB solution (100 mL, 7 mg/L) with 0.3 g/L photocatalyst was stirred in dark for 30 min to make sure that the system reached adsorption-desorption equilibrium. And a distance of 15 cm was kept between the light source and the liquid level of RhB aqueous solution. During irradiation, 2.5 mL RhB solution was sampled at certain intervals and the catalyst was separated by using a magnet. Subsequently, the maximum absorbance of RhB solution at 555 nm was recorded using an UV–vis spectrophotometer (UV-5800PC, Shanghai Metash Instruments Co., Ltd). The photocatalytic degradation process was calculated using the equation: $C/C_0 = A/A_0$, where C_0 and C are the initial and real time concentrations of RhB solution, and A_0 and A represent the initial and real-time absorbance of RhB solution.

3. Result and discussion

3.1. Morphologies and phase structures

Morphologies and microstructures of the as-prepared samples were studied by FESEM and TEM measurements. The SEM and TEM images for F, FS, FSz and FSZ samples are presented in Fig. 1. As shown in Fig. 1a1 and a2, pure F particles possess rough surface and regular sphere-shaped morphology with an average diameter of 240 nm. Fig. 1b1 reveals that FS particles have the same morphological properties with pure F particles, except for a smoother surface and a slightly larger size about 280 nm. It can be clearly seen from Fig. 1b2 that FS particles present a core-shell structure including black F sphere as core and gray color SiO_2 shell with a thickness of 20 nm on average. When ZnO seeds are loaded on FS spheres, as displayed in Fig. 1c1, a uniform ZnO seed-coating wraps on FS microsphere forming a rough surface and no apparent aggregation of the FSz microspheres can be observed. TEM image in Fig. 1c2 presents the detailed morphology of FSz microspheres, which displays a typical three-layer structure composed of a F core, a SiO_2 interlayer and a ZnO seed-layer with a thickness of about 5 nm. In the case of FSZ sample, it can be seen from Fig. 1d1 that all these FSz microspheres are totally enwrapped by ZnO nanorods and the chestnut-like FSZ microspheres are obtained. The average length and diameter of ZnO nanorods are about 150 nm and 23 nm, respectively, which can be determined by the TEM image in Fig. 1d2.

Fig. 2 displays the morphology and distribution of Au NPs supported on ZnO nanorod-layer for four kinds of FSZA microsphere. As shown in Fig. 2a1, when 5 mL of $HAuCl_4 \cdot 4H_2O$ solution was used, FSZA1 microsphere possesses the similar morphological properties as with the original FSZ microsphere. But, it can be clearly appreciated from Fig. 2a2 that Au NPs with a diameter of approximately 4 nm are sparsely and uniformly adhered to the surface of ZnO nanorod-layer. After increasing the amount of $HAuCl_4 \cdot 4H_2O$ solution (15 ml) for the first time, there are no obvious differences between FSZA1 and FSZA2 microspheres by contrasting Fig. 2a1 and b1. TEM image in Fig. 2b2 shows evidently that the surface of FSZA2 microsphere loads more Au NPs than FSZA1 microsphere. By increasing the dosage of $HAuCl_4 \cdot 4H_2O$ solution to 25 mL, as presented in Fig. 2c1, the surfaces of ZnO nanorods on FSZA3 microsphere become rough and the diameter of this ZnO nanorod is about 30 nm, which can be ascribed to the substantially enhanced quantity of Au NPs as given in Fig. 2c2. As shown in Fig. 2d1 and d2, when the dosage of $HAuCl_4 \cdot 4H_2O$ solution is further increased to 35 mL, not only more Au NPs deposit on the surface of ZnO nanorod-layer of FSZA3 microsphere, but also some Au NPs become larger due to the aggregation of freshly generated Au particles on previously formed ones. Besides, the ZnO nanorods of FSZA4 microsphere are shorter than initial ZnO nanorods, which may be related to the use of a large amount of weakly acid $HAuCl_4 \cdot 4H_2O$ solution.

Fig. 3a is TEM image of single FSZA3 microsphere, and corresponding HRTEM image is given in Fig. 3b. The HRTEM image for selected area of this FSZA3 microsphere displays individual Au NPs closely attached onto the ZnO nanorod, suggesting their strong binding. In addition, two types of lattice fringes with spacing of about 0.260 and 0.236 nm can be indexed to the (002) plane of the hexagonal crystal structure of ZnO (JCPDS card No. 36-1451) and the (111) plane of face-centered cubic Au (JCPDS card No. 04-0781), respectively. This further reveals that the ZnO-Au heterostructure formed on the surfaces of FSZA3 core-shell microspheres. The elemental mapping images with different color in Fig. 3c–g indicate Fe, Si, O, Zn, and Au enriched areas of a single FSZA3 microsphere, respectively. The Fe signal is located in the center of the microsphere and gradually surrounded by Si, O, Zn and Au signals, which clearly demonstrate that the formation of excepted FSZA3 core-shell structure.

The phase structure and purity of the as-prepared samples were identified by XRD measurements. Fig. 4a shows the XRD pattern of the obtained F product, the diffraction peaks appear at $2\theta = 30.10°$,

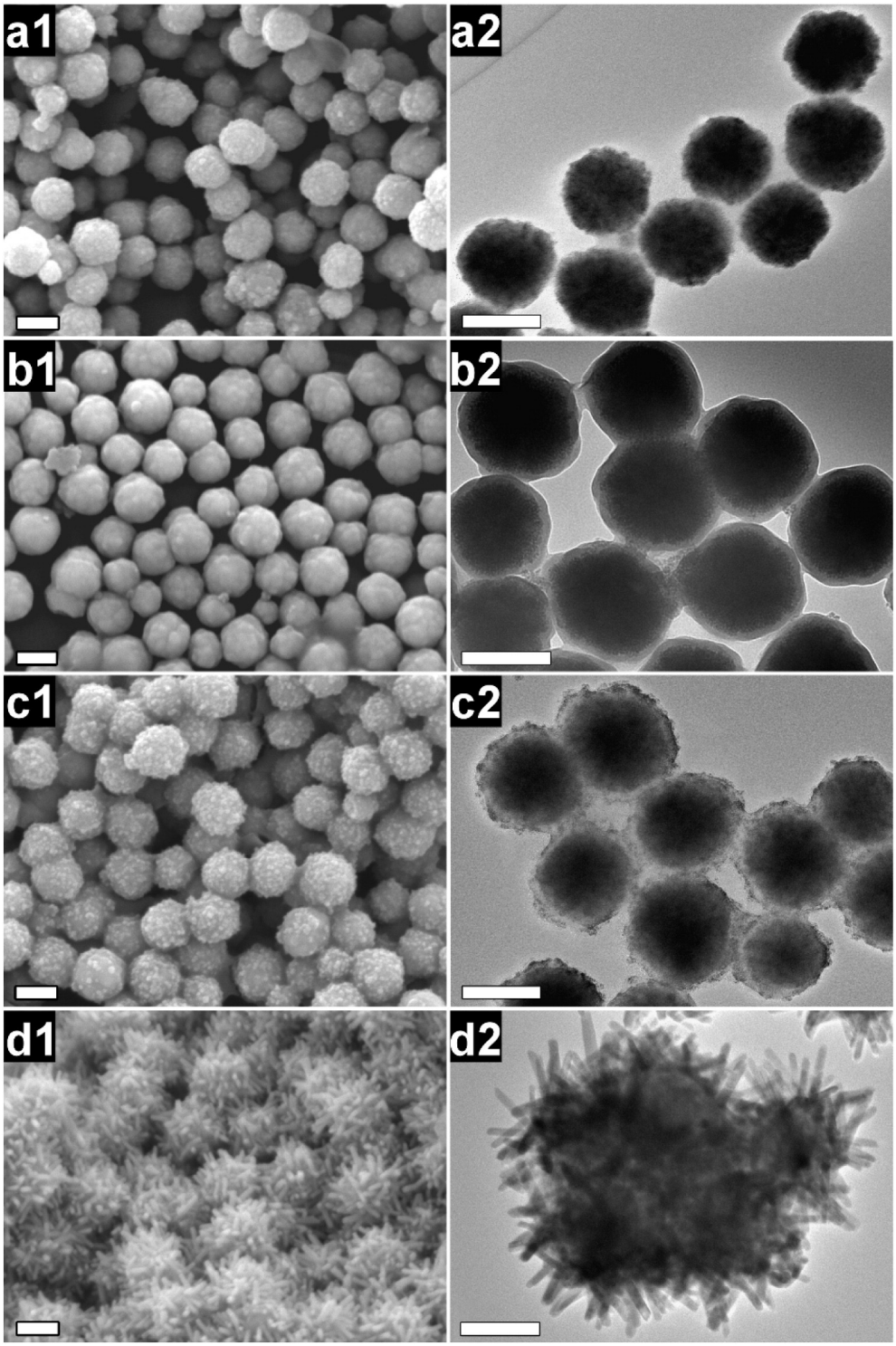

Fig. 1. SEM and TEM images of the as-prepared samples: (a1–2) F, (b1–2) FS, (c1–2) FSz and (d1–2) FSZ. (All scale bars are 200 nm).

35.42°, 43.05°,53.59°, 56.94°, 62.52° and 73.95°, which are assigned to (220), (311), (400), (422), (511), (440) and (533) crystal planes of magnetite Fe_3O_4 (JCPDS card No. 19-0629). The XRD pattern of FS sample (Fig. 4b) exhibits the same feature as pure F sample, indicating the coated SiO_2 shell is amorphous. After coating ZnO seeds on the surface of the FS microspheres, a very tiny peak emerges at 31.77° in Fig. 4c, which can be indexed to the (100) crystal plane of hexagonal ZnO (JCPDS card No. 36-1451). Noticeably, with regard to FSZ sample, several new peaks emerges at 34.42°, 36.25°, 47.54°, 56.60°, 62.86°, 66.38°, 67.96, 69.10°, 72.56° and 76.96° in Fig. 4d. Those peaks can also be indexed to the hexagonal wurtzite ZnO. In the case of FSZA3, besides the characteristic diffraction of Fe_3O_4 and ZnO, the diffraction peaks at $2\theta = 37.9°$ and 44.1° in Fig. 4e can be attributed to face-centered-cubic structured Au (JCPDS card No. 04-0781), suggesting crystallized Au NPs have been deposited on the outer shell.

3.2. Magnetic properties

Magnetic hysteresis loops of the as-synthesized products were measured in the range of −15.0 to 15.0 kOe magnetic fields as plotted in

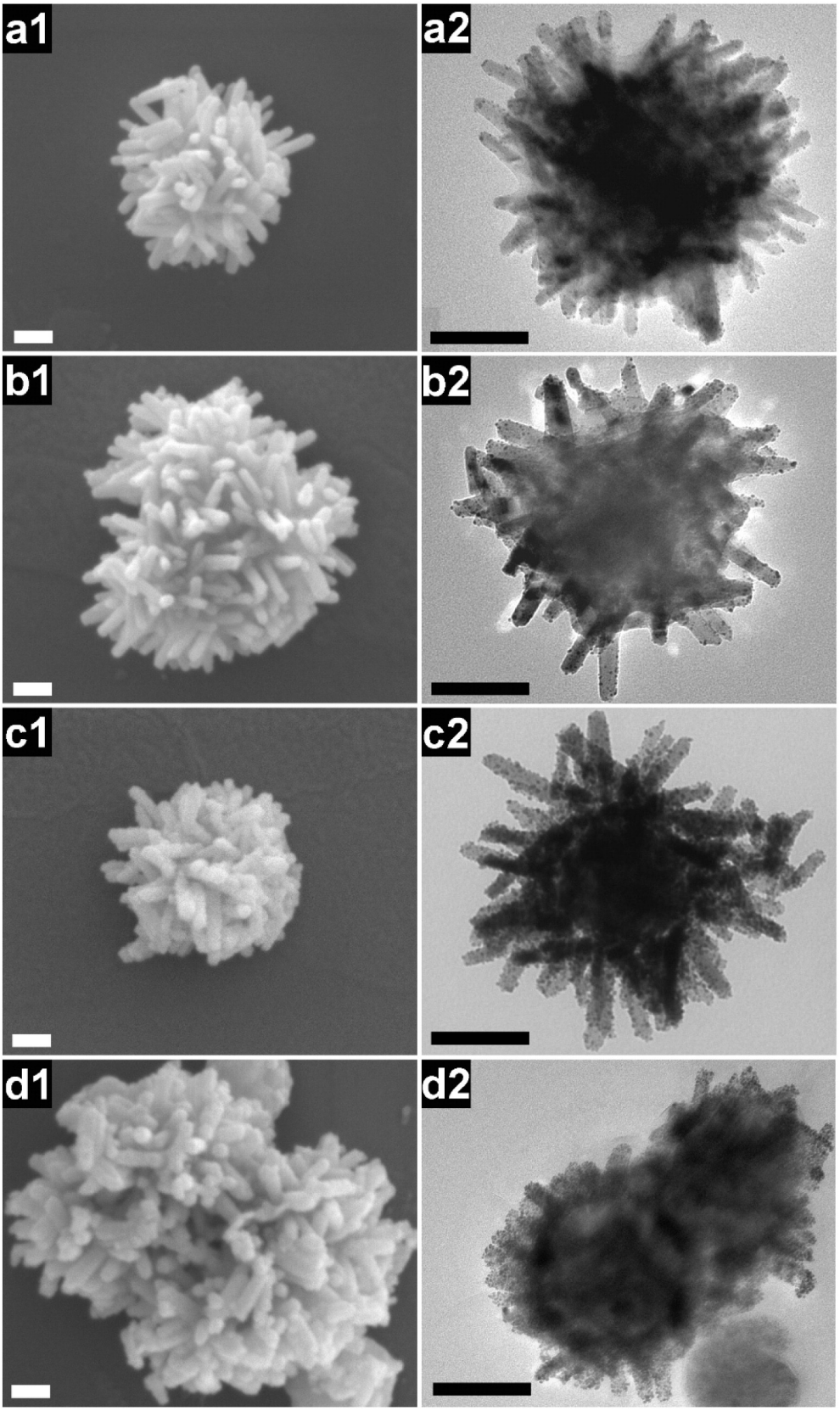

Fig. 2. SEM and TEM images of FSZA samples with different amounts of Au NPs: (a1–2) FSZA1, (b1–2) FSZA2, (c1–2) FSZA3 and (d1–2) FSZA4. (All scale bars are 100 nm).

Fig. 5a. The saturation magnetization (Ms) value of original F is 62.55 emu/g. After the subsequent coating process, the MS values decrease to be 53.01, 46.97, 36.57, 30.79, 28.86, 27.27 and 23.67 emu/g for FS, FSz, FSZ, FSZA1, FSZA2, FSZA3 and FSZA4 microspheres, respectively. The lower Ms values of the F based core-shell microspheres (FS, FSz, FSZ, FSZA1, FSZA2, FSZA3 and FSZA4) are mainly due to the non-

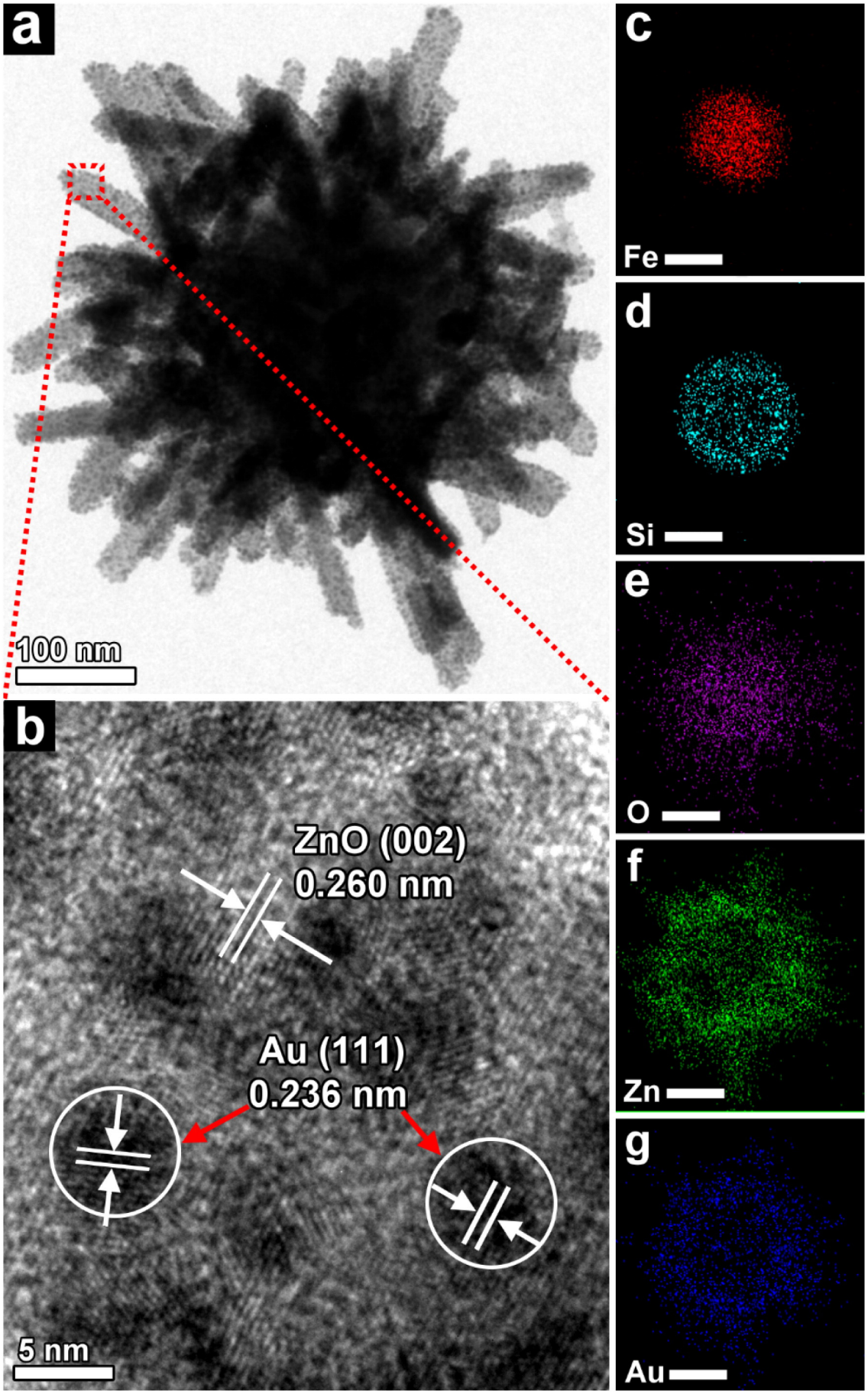

Fig. 3. (a) TEM image of a single FSZA3 microsphere. (b) HRTEM image for the selected area in (a). (c–g) Elemental mapping images of a single FSZA3 microsphere (all scale bars are 100 nm).

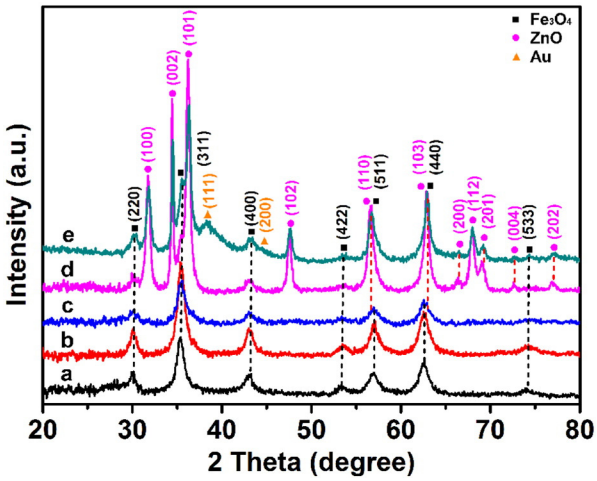

Fig. 4. XRD patterns of different products: (a) F, (b) FS, (c) FSz, (d) FSZ and (e) FSZA3.

magnetic SiO_2, ZnO and Au content in these microspheres. Moreover, it can be seen from Fig. 5a that all magnetic hysteresis loops do not show any significant remanent magnetization and coercivity, suggesting superparamagnetic feature of the examined samples.

The above analysis indicates that all as-prepared FSZA samples possess excellent magnetic properties. With the help of an external magnetic field, such excellent magnetic properties facilitate the cyclic utilization of these microspheres. As shown in Fig. 5b and c, although the Ms value of the FSZA4 microspheres is the lowest among all samples, the complete magnetic separation can be achieved in 60 s by placing a magnet near the vessels containing the aqueous dispersion of FSZA4 microspheres. After removing the magnet (Fig. 5d), the FSZA4 sample is quickly redispersed in the aqueous solution by shaking. In this regard, this almost negligible residual magnetism avoided forming magnetized clumps in liquid medium. Therefore, the superparamagnetic behaviors would facilitate the cyclic utilization of FSZA composite materials by applying an appropriate magnetic field.

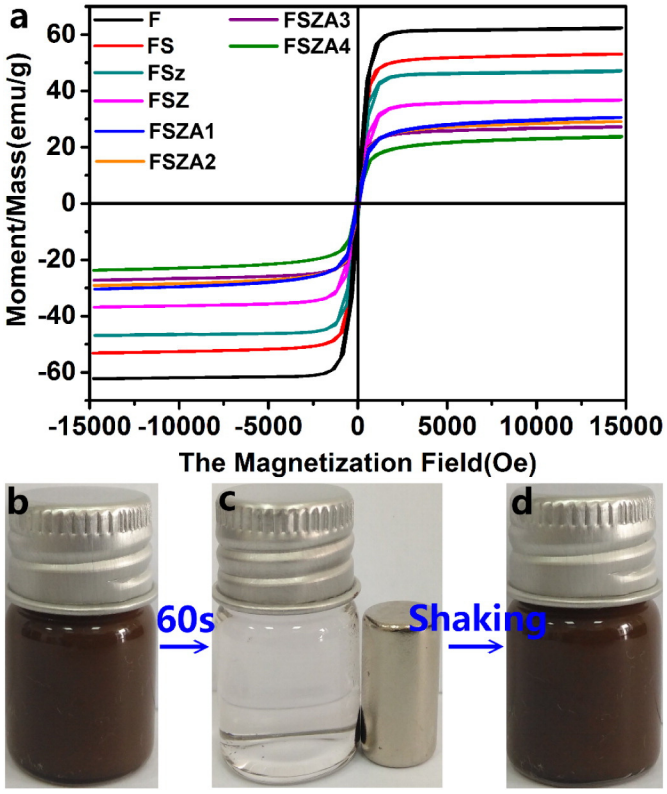

Fig. 5. (a) Magnetic hysteresis loops of the products at room temperature. (b–d) Photographs of FSZA4 aqueous solution after magnetic separation and shaking.

3.3. N_2-sorption

To determine the textural properties of the samples, including nature of porosity and BET-surface area, N_2 adsorption-desorption measurements were performed. Fig. 6a shows the N_2 adsorption-desorption isotherms of various samples. The desorption branches do not reach the adsorption branches, attesting the presence of porosity in tested samples [27]. And the tested materials exhibit high adsorption at relative pressures P/P_0 close to 1.0, suggesting the formation of mesopores (2.0–50.0 nm) and macropores (>50.0 nm) [28]. This is further confirmed by pore-size distribution curves of the different samples as given in Fig. 6b. By using the Barrett-Joyner-Halenda (BJH) method and the desorption branch, the tested microspheres mainly contain mesopores and macropores. The mesopores come from slitlike pores within ZnO layer consisting of dense and uniform nanorods. The macropores reflect the pores formed between stacked microspheres.

The BET analysis in Fig. 6c shows a surface area of 25.65, 29.93, 43.18, 57.90 and 24.51 m^2/g for FSZ, FSZA1, FSZA2, FSZA3 and FSZA4 samples, respectively. With the increase of Au NPs, the specific surface area of FSZA series samples increases gradually. However, the specific surface area of FSZA4 is far less than that of FSZA3 sample, which is related to its morphological characters as depicted in TEM image of Fig. 2d2, including the shorter ZnO nanorods and the agglomeration of Au NPs. The above result indicates that varying the loaded amount of Au NPs significantly affect the specific surface area and pore size distribution of obtained products. With a large specific surface area, the FSZA3 sample has great promise in not only facilitating the transfer of photogenerated carriers, but also offering sufficient interfacial area for adsorbing the RhB molecules to ultimately improve photocatalytic performance [5].

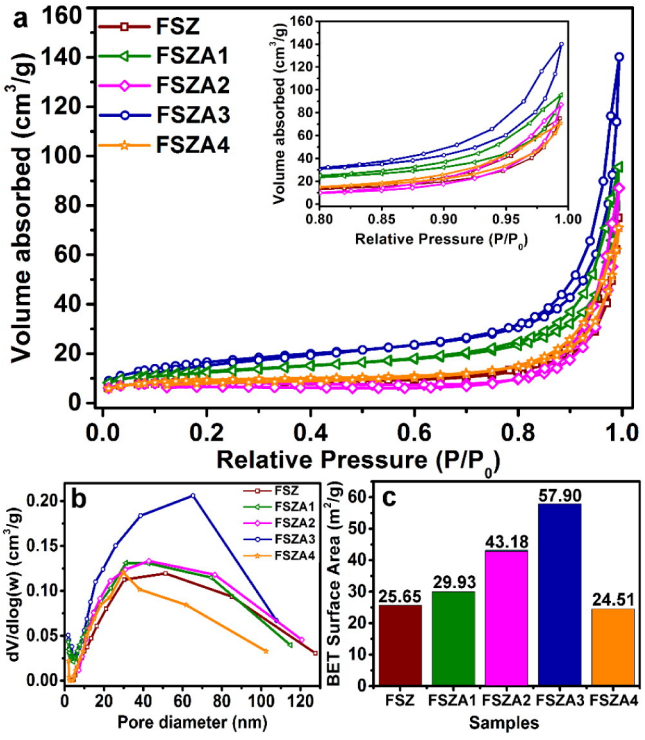

Fig. 6. (a) N_2 adsorption-desorption isotherms of various samples. Inset: the magnified region in order to view adsorption-desorption hysteresis loops corresponding to different samples. (b) Pore size distribution curves and (c) BET special surface for various samples.

3.4. Photocurrent properties

To investigate the photoinduced behavior of the generated photocurrent response of samples, the amperometric i-t curves obtained in the dark and under UV light irradiation, are given in Fig. 7. All the samples show a negligible current response in the dark. In contrast, upon illumination, all tested samples show a speedy response and a steady-state current is obtained. The rise time and fall time of photocurrent for FSz, FSZ and various FSZA samples are given in Table 1. It can be seen that the rise and fall times of all tested samples is transient. The prompt increase in photocurrent response from light-off to light-on state is mainly ascribed to the quick interfacial charge transportation of between the samples and the electrolyte [29]. Moreover, all of the tested samples show reproducible photocurrent generation in response to illumination, and there is no obvious current drop after 200 s of testing.

Interestingly, the generated transient photocurrents of various samples are evidently different. The photocurrent density of various samples increases in the order: FSz (1.97 μA) < FSZA4 (2.30 μA) < FSZ (3.38 μA) < FSZA1 (5.93 μA) < FSZA2 (7.88 μA) < FSZA3 (19.37 μA). The photocurrent of the FSz is lowest due to its less ZnO content. The photocurrent of the FSZ, FSZA1, FSZA2 and FSZA3 samples increases gradually as the content of Au NPs is increased, after which it begins to decline with further increase in the content of Au NPs. The lower photocurrent of the FSZA4 sample with respect to FSZ indicates that the increased aggregation of Au NPs can induce new recombination centers, and inhibit further generation of electrons and holes [30]. It is well known that higher photocurrent is corresponding to more photo-generated carriers [8]. Here, the formation of a ZnO/Au heterojunction facilitating electron transfer, which accelerates the separation of photo-generated charge carriers. Thus, the appropriate loading of Au NPs would be beneficial for the improvement of photocatalytic activity.

3.5. Photocatalytic capacities

The photocatalytic activities of the different samples are evaluated by photodegradation of RhB under UV light, which is a typical organic azo-dye pollutant in the textile industry. The corresponding RhB degradation efficiencies as a function of time are demonstrated in Fig. 8a. In addition, because of the photodegradation process complies with the pseudo-first-order kinetics, the equation $-\ln(C/C_0) = kt$ is used to fit the experimental date, where k is the apparent rate constant, and the k values for the different photocatalysts are given in Fig. 8b. In the blank test (without catalysts), the concentration of RhB changes little after irradiation for 80 min, indicating the self-decomposition of RhB can be neglected. The photocatalytic efficiency of various samples estimated follows the order: FSZA3 > FSZA2 > FSZA1 > FSZ > FSZA4 > FSz. The FSz microspheres exhibit the lowest photocatalytic activity and the photodegradation rate of RhB is only 27.13%, which is mainly due to large mass proportion of inactive FS in FSz samples with a small amount of ZnO seeds. For FSZ microspheres, the adequate space between the ZnO nanorods structure is ideal for fast electron transportation, adsorption of pollutants and transformation of degraded products [3]. Therefore, the degradation efficiency of RhB for FSZ sample is significantly enhanced and about 60.73%. And the k value for FSZ microspheres is about 2.6 times that of FSz microspheres. When FSZA photocatalytic systems are used under the same condition, the photodegradation rates of RhB for FSZA1, FSZA2, FSZA3 and FSZA4 microspheres are 67.72%, 84.10%, 93.54%, and 34.13%, respectively, and the k value of 0.03134 min^{-1} for FSZA3 microspheres is the biggest. Above tested result indicates the photocatalytic efficiency of FSZA series sample does not enhanced linearly with the increase in load quantity of Au NPs. Instead, the photocatalytic efficiency of FSZA4 sample is weaker than FSZ sample, which is in accord with the result of photocurrent.

Table 1
The rise time and fall time of photocurrent for FSz, FSZ and various FSZA samples.

Sample	FSz	FSZ	FSZA1	FSZA2	FSZA3	FSZA4
Rise time (s)	0.85	0.76	0.69	0.45	0.34	0.55
Fall time (s)	1.22	1.15	1.09	0.99	0.89	0.99

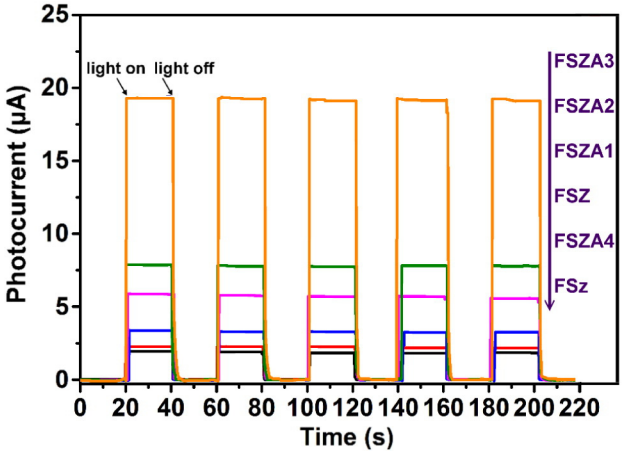

Fig. 7. Photocurrent responses of FSz, FSZ and various FSZA samples.

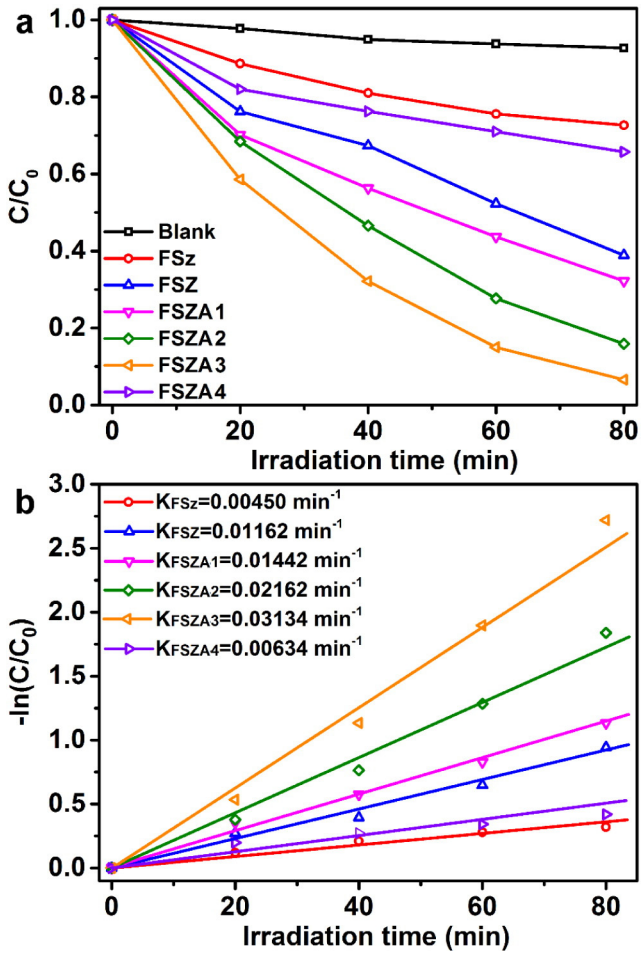

Fig. 8. (a) Photocatalytic degradation of RhB in the presence of different catalysts. (b) Pseudo-first order kinetic curves for the photodegradation of RhB by various photocatalysts.

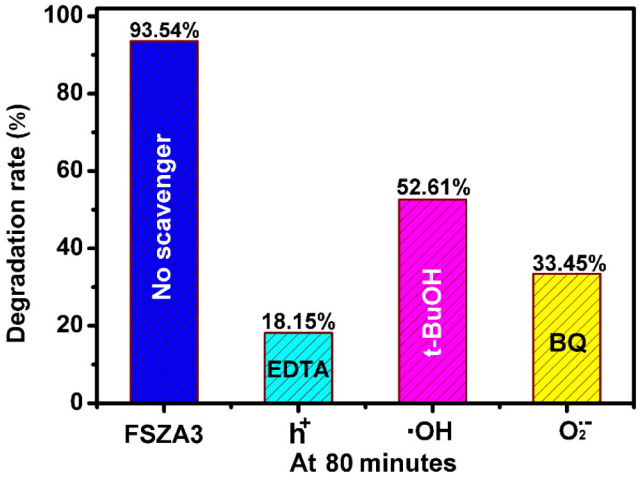

Fig. 9. Effect of active species scavengers on percentage photodegradation of RhB using FSZA3 photocatalyst under UV light irradiation.

3.6. Photocatalysis mechanism of FSZA microspheres

To investigate the active species involved in the photocatalytic process, the radical trapping experiment was performed by adding ethylenediaminetetraacetate (EDTA), *tert*-butyl alcohol (*t*-BuOH), and 1,4-benzoquinone (BQ) to scavenge h^+, •OH, and O_2•$^-$, respectively. The radical trapping experiment procedure was similar to the degradation experiment; different scavengers were separately introduced into the aqueous RhB before the addition of FSZA3 photocatalyst. Fig. 9 shows the results of radical trapping experiment. After adding EDTA, *t*-BuOH and BQ scavengers, the degradation rate of RhB decreases from 93.54% (no scavenger) to 18.15% (EDTA), 52.61% (*t*-BuOH), and 33.45% (BQ), respectively. Above dates demonstrate that h^+, •OH, and O_2•$^-$ are the primary reactive species associated with the enhanced photocatalytic activity of FSZA3 photocatalyst.

In addition, a plausible photocatalytic mechanism of FSZA series samples is illustrated in detail. As depicted in Scheme 2, when FSZA microspheres are irradiated by UV light, the photoelectrons transfer to the conduction band (CB) of ZnO from the valence band (VB) of ZnO, leaving behind a chemically-equivalent number of holes in this VB. Since the Fermi energy level of Au is lower than the bottom of the CB of ZnO, quick transfer of photoelectrons from ZnO nanorods to Au NPs takes place, which continues until the new Fermi energy level of the ZnO/Au heterogeneous nanostructures forms. Here, Au NPs act as electron trappers that effectively facilitate the separation of photoinduced electron-hole pairs. In addition, the electron transfer from the ZnO surface to adsorbed O_2 is believed to be a rate-limiting step in photocatalytic reactions [12]. For FSZA series samples, Au NPs that adjacent to interfacial O_2 adsorption sites can lower the local work function of ZnO. Thus, it results in a significant increase at the rate of electron transfer to O_2 [10]. However, when overloading too much Au NPs on ZnO nanorod-layer, the excessive Au NPs not only decrease the effective catalytic sites on the surface of ZnO nanorods, but also form Au aggregations that would inhibit the diffusion and mass transportation of the reactants molecules, products molecules, and reactive species generated during the photochemical process. It can be seen that the loaded amount of Au NPs is vital for a balance between two opposed functions of Au NPs in photocatalysis. And FSZA3 sample is the best catalyst among four kinds of FSZA sample based on the photocatalytic test results. Above all, it is not difficult to understand why FSZA1, FSZA2, and FSZA3 samples are superior to FSZ, while FSZA4 sample is weaker than FSZ sample in photocatalytic activity.

3.7. Reusability of FSZA3 photocatalyst

The cyclic stability of FSZA3 photocatalyst was investigated by monitoring the catalytic activity during successive five cycles of use. As shown in Fig. 10a, the photodecolorization efficiency of FSZA3 catalyst decreases slightly in multiple photocatalytic experiments, suggesting the well-designed FSZA3 sample possess excellent photocatalytic stability. Additionally, the FSZA3 photocatalyst was recycled with the help of an external magnetic field after each cycle, indicating FSTA3 also has stable magnetic properties. Fig. 10b shows the magnetic hysteresis loops of FSZA3 sample before and after five times of photocatalytic test. The almost no change in Ms value confirms that the magnetic stability of FSZA3 photocatalyst. The SEM and TEM images of FSZA3 sample after five cycles of photocatalytic test are displayed in Fig. 10c and d, respectively. Obviously, the FSZA3 sample maintains the primary microstructure, suggesting FSZA3 photocatalyst is mechanically stable.

To further determine the stability in surface compositions and bonding environment, FSZA3 sample before and after 5 cycles of photocatalytic test was measured by XPS analyses. The XPS fully scanned spectra of FSZA3 before and after RhB discoloration are given in Fig. 11a. The Zn, Au, O 1s and C 1s peaks appear in fully scanned spectra of both tested samples. The C 1s peak at 284.6 eV is attributed to the adventitious carbon-based contaminant. As XPS is a highly surface-specific technique with a typical analysis depth of about 10 nm. No signal of Fe and Si elements on both fully scanned spectra can be found, suggesting FS cores are absolutely wrapped in the center of FSZA3 microspheres before and after multiple photocatalytic tests.

The corresponding high resolution XPS patterns of Zn 2p are presented in Fig. 11b, and the photoelectron peaks of Zn $2p_{3/2}$ and Zn

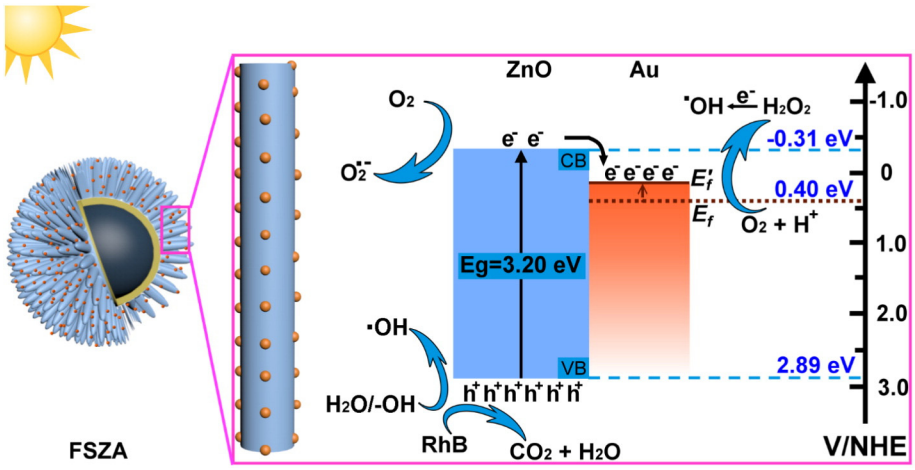

Scheme 2. Schematic diagram for the proposed photodegradation mechanism of RhB by FSZA catalysts.

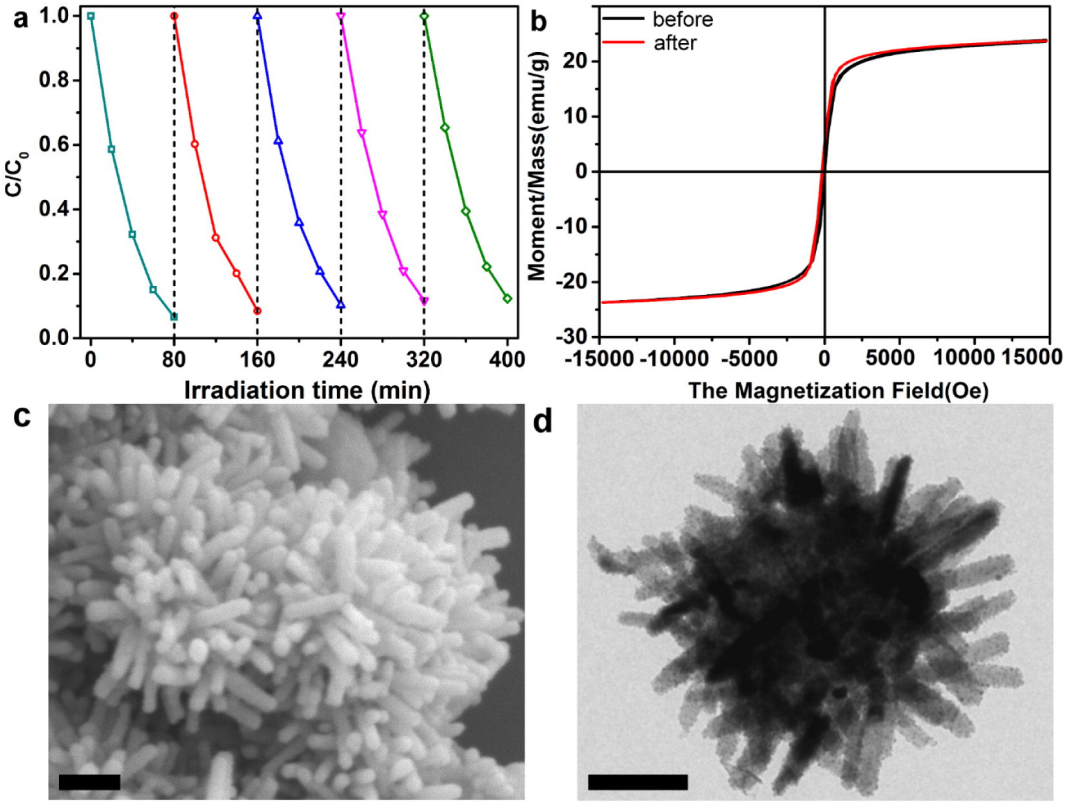

Fig. 10. (a) Five cycles of the photocatalytic degradation of RhB in the presence of FSZA3 sample. (b) Magnetic hysteresis loop of FSZA3 sample before and after five cycles of photocatalytic test. (c) SEM image and (d) TEM image of FSZA3 sample after five cycles of photocatalytic test. (All scale bars are 100 nm).

$2p_{1/2}$ are located at 1020.8 and 1044.0 eV, respectively. The spin orbit separation of 23.2 eV indicates the Zn element exists in the form of Zn^{2+} of ZnO in tested samples. As depicted in Fig. 11c, both XPS spectra of O 1 s can be divided into two peaks. The peak at 528.8 eV can be attributed to the binding of O^{2-} ions and Zn^{2+} in hexagonal wurtzite ZnO, whereas the peak at 530.4 eV is ascribed to O^{2-} ions that are in

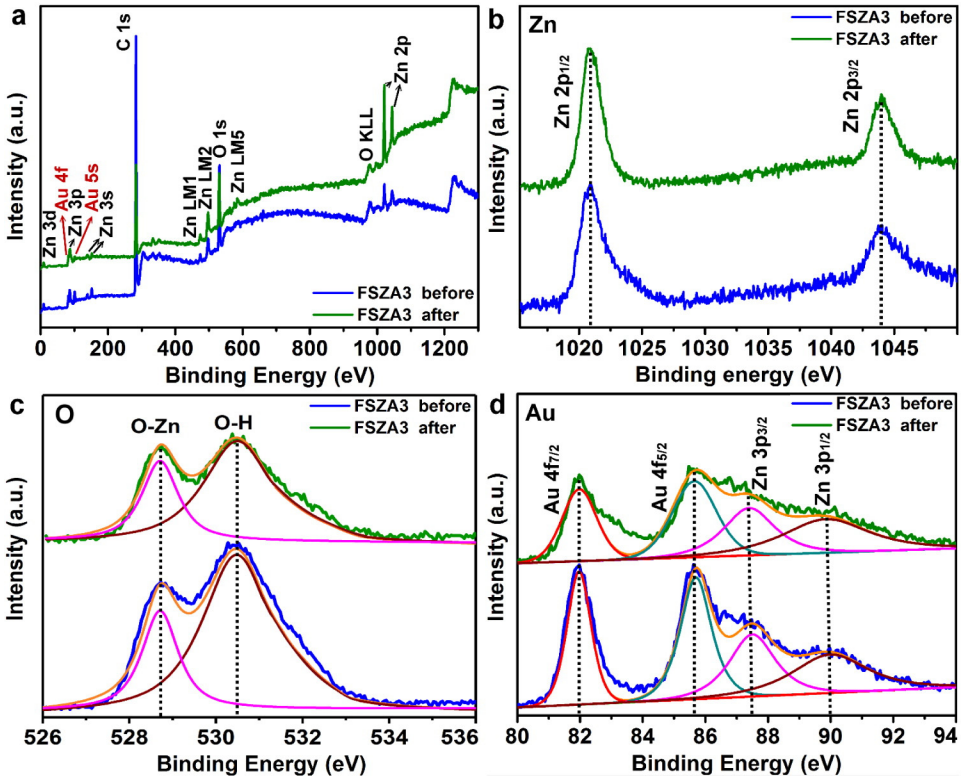

Fig. 11. (a) XPS fully scanned spectra, (b) XPS spectra of Zn 2p, (c) XPS spectra of O 1s and (d) XPS spectra of Au 4f for FSZA3 sample before and after five cycles of photocatalytic test.

oxygen deficient regions within the matrix of ZnO and Zn-OH groups [31]. As can be seen from Fig. 11d, the high resolution XPS pattern of Au element exhibits the Au 4f7/2 and 4f5/2 doublets with the binding energies of 81.9 eV and 85.7 eV, respectively. Two peaks of this Au NPs are negatively shifted compared to bulk Au, which is related to electron migration between Fermi energies of ZnO and Au NPs [32]. The spin orbit separation of 3.8 eV for Au $4f_{7/2}$ and $4f_{5/2}$ doublets is a typical value for Au^0, suggesting Au NPs exist on the surface of FSZA3 microspheres before and after multiple photocatalytic test [17]. In addition, Fig. 11d presents two extra overlapping shoulders at 87.4 and 89.9 eV. According to the National Institute of Standards and Technology (NIST) XPS database, both characteristic peaks can be assigned to Zn $3p_{3/2}$ and Zn $3p_{1/2}$, respectively. Overall, before and after five cycles of photocatalytic test, the high resolution XPS patterns of Zn, O and Au for FSZA3 sample almost have no change, further showing that the FSZA3 microspheres possesses good chemically stability.

4. Conclusions

Herein, an effective route to synthesize magnetically separable Fe_3O_4@SiO_2@ZnO@Au microspheres with core-shell structure and enhanced photocatalytic activity was described. And four kinds of Fe_3O_4@SiO_2@ZnO@Au microsphere with different amount of Au nanoparticles were controlled prepared for comparison. The enhanced photocatalytic property was demonstrated to be derived from two main reasons: on the one hand, the ZnO nanorod-layer uniformly and precisely grew on Fe_3O_4@SiO_2 surface, enhancing the level of photocatalytic activity owing to the larger specific surface area; on the other hand, the modification of an optimum amount of Au nanoparticles on Fe_3O_4@SiO_2@ZnO microspheres improved the separation of photoinduced electron-holes. Moreover, this Fe_3O_4@SiO_2@ZnO@Au photocatalyst showed excellent stability and recyclability during five cycles. The high photocatalytic activity, efficient magnetic separation, good stability in chemistry and mechanics make the Fe_3O_4@SiO_2@ZnO@Au photocatalyst a promising candidate for environmental-friendly water purification. Meanwhile, this study provides a new route for the controlled fabrication of multifunctional photocatalytic nanosystems with a broad application prospect.

Acknowledgments

This work is supported by the National Natural Science Foundation of China (Grant Nos. 61378085, 51479220, 61775081, 51608226 and 61705079).

References

[1] L.M. Fernandez, A.S. Fernandez, G.F. Carrasco, O. Miloševic, M.E. Rabanal, Solvothermal synthesis of Ag/ZnO micro/nanostructures with different precursors for advanced photocatalytic applications, Adv. Powder Technol. 28 (2017) 83–92.
[2] A.G. Shiravizadeh, R. Yousefi, S.M. Elahi, S.A. Sebt, Effects of annealing atmosphere and rGO concentration on optical properties and enhanced photocatalytic performance of SnSe/rGO nanocomposites, Phys. Chem. Chem. Phys. 19 (2017) 18089–18098.
[3] X. Bian, K. Hong, X. Ge, R. Song, L. Liu, M. Xu, Functional hierarchical nanocomposites based on ZnO nanowire and magnetic nanoparticle as highly active recyclable photocatalysts, J. Phys. Chem. C 119 (2015) 1700–1705.
[4] L. Amidani, A. Naldoni, M. Malvestuto, M. Marelli, P. Glatzel, V. Dal Santo, F. Boscherini, Probing long-lived plasmonic-generated charges in TiO_2/Au by high-resolution X-ray absorption spectroscopy, Angew. Chem. Int. Ed. 54 (2015) 5413–5416.
[5] H.R. Azimi, M. Ghoranneviss, S.M. Elahi, M.R. Mahmoudian, F. Jamali-sheini, R. Yousefi, Excellent photocatalytic performance under visible-light irradiation of ZnS/rGO nanocomposites synthesized by a green method, Front. Mater. Sci. 10 (2016) 385–393.
[6] L. Wang, G. Tian, Y. Chen, Y. Xiao, H. Fu, In situ formation of a ZnO/ZnSe nanonail array as a photoelectrode for enhanced photoelectrochemical water oxidation performance, Nanoscale 8 (2016) 9366–9375.
[7] J.M. Li, H.Y. Cheng, Y.H. Chiu, Y.J. Hsu, ZnO–Au–SnO_2 Z-scheme photoanodes for remarkable photoelectrochemical water splitting, Nano 8 (2016) 15720–15729.
[8] X. Liu, Z. Li, W. Zhao, C. Zhao, J. Yang, Y. Wang, Zinc oxide nanorod/Au composite arrays and their enhanced photocatalytic properties, J. Colloid Interface Sci. 432 (2014) 170–175.
[9] A. Kharatzade, F. Jamali-Sheini, R. Yousefi, Excellent photocatalytic performance of Zn(1-x)MgxO/rGO nanocomposites under natural sunlight irradiation and their photovoltaic and UV detector applications, Mater. Des. 107 (2016) 47–55.
[10] L. Zu, Y. Qin, J. Yang, In situ synergistic crystallization-induced synthesis of novel Au nanostar-encrusted ZnO mesocrystals with high-quality heterojunctions for high-performance gas sensors, J. Mater. Chem. A 3 (2015) 10209–10218.
[11] X.Z.X.H. Wang, W.Z. Cheng, H.Q. Shao, X. Liu, X.M. Li, H.L. Liu, A.J. Wu, Facile synthesis and optical properties of polymer-laced ZnO–Au hybrid nanoparticles, Nanoscale Res. Lett. 9 (109) (2014) 1–7.
[12] X. Hou, L. Wang, Controllable fabrication and photocatalysis of ZnO/Au nanohybrids via regenerative ion exchange and reduction cycles, RSC Adv. 4 (2014) 56945–56951.
[13] B.H. Nguyen, V.H. Nguyen, Recent advances in research on plasmonic enhancement of photocatalysis, Adv. Nat. Sci. Nanosci. Nanotechnol. 6 (2015) 043001.
[14] A. Senthilraja, B. Subash, B. Krishnakumar, D. Rajamanickam, M. Swaminathan, M. Shanthi, Synthesis, characterization and catalytic activity of co-doped Ag–Au–ZnO for MB dye degradation under UV-A light, Mater. Sci. Semicond. Process. 22 (2014) 83–91.
[15] H.B. Zeng, W.P. Cai, P.S. Liu, X.X. Xu, H.J. Zhou, C. Klingshirn, H. Kalt, ZnO-based hollow nanoparticles by selective etching elimination and reconstruction of metal-semiconductor interface improvement of blue emission and photocatalysis, ACS Nano 2 (2008) 1661–1670.
[16] S. Sarkar, A. Makhal, T. Bora, S. Baruah, J. Dutta, S.K. Pal, Photoselective excited state dynamics in ZnO–Au nanocomposites and their implications in photocatalysis and dye-sensitized solar cells, Phys. Chem. Chem. Phys. 13 (2011) 12488–12496.
[17] S. Zhu, S. Liang, Q. Gu, L. Xie, J. Wang, Z. Ding, P. Liu, Effect of Au supported TiO_2 with dominant exposed {001} facets on the visible-light photocatalytic activity, Appl. Catal. B Environ. 119–120 (2012) 146–155.
[18] J.F. Fernando, M.P. Shortell, C.J. Noble, J.R. Harmer, E.A. Jaatinen, E.R. Waclawik, Controlling Au photodeposition on large ZnO nanoparticles, ACS Appl. Mater. Interfaces 8 (2016) 14271–14283.
[19] M. Shekofteh-Gohari, A. Habibi-Yangjeh, Photosensitization of Fe_3O_4/ZnO by AgBr and Ag_3PO_4 to fabricate novel magnetically recoverable nanocomposites with significantly enhanced photocatalytic activity under visible-light irradiation, Ceram. Int. 42 (2016) 15224–15234.
[20] D.D. Wang, J.H. Yang, X.Y. Li, H.J. Zhai, J.H. Lang, H. Song, Preparation of magnetic Fe_3O_4@SiO_2@mTiO_2-Au spheres with well-designed microstructure and superior photocatalytic activity, J. Mater. Sci. 51 (2016) 9602–9612.
[21] S. Abramson, L. Srithammavanh, J.M. Siaugue, O. Horner, X.Z. Xu, V. Cabuil, Nanometric core-shell-shell γ-Fe_2O_3/SiO_2/TiO_2 particles, J. Nanopart. Res. 11 (2008) 459–465.
[22] X. Li, D. Liu, S. Song, H. Zhang, Fe_3O_4@SiO_2@TiO_2@Pt hierarchical core-shell microspheres: controlled synthesis, enhanced degradation system, and rapid magnetic separation to recycle, Cryst. Growth Des. 14 (2014) 5506–5511.
[23] C. Wang, L. Yin, L. Zhang, L. Kang, X. Wang, R. Gao, Magnetic (γ-Fe_2O_3@SiO_2)n@TiO_2 functional hybrid nanoparticles with actived photocatalytic ability, J. Phys. Chem. C 113 (2009) 4008–4011.
[24] X.X. Yu, S.W. Liu, J.G. Yu, Superparamagnetic γ-Fe_2O_3@SiO_2@TiO_2 composite microspheres with superior photocatalytic properties, Appl. Catal. B Environ. 104 (2011) 12–20.
[25] D.D. Wang, J.H. Yang, X.Y. Li, J. Wang, H.J. Zhai, J.H. Lang, H. Song, Effect of thickness and microstructure of TiO_2 shell on photocatalytic performance of magnetic separable Fe_3O_4/SiO_2/mTiO_2 core-shell composites, Phys. Status Solidi A 1600665 (2017) 1–8.
[26] J.H. Yang, J. Wang, X.Y. Li, D.D. Wang, H. Song, Synthesis of urchin-like Fe_3O_4@SiO_2@ZnO/CdS core-shell microspheres for the repeated photocatalytic degradation of rhodamine B under visible light, Catal. Sci. Technol. 6 (2016) 4525–4534.
[27] H. Moussa, E. Girot, K. Mozet, H. Alem, G. Medjahdi, R. Schneider, ZnO rods/reduced graphene oxide composites prepared via a solvothermal reaction for efficient sunlight-driven photocatalysis, Appl. Catal. B Environ. 185 (2016) 11–21.
[28] B. Chouchene, T.B. Chaabane, L. Balan, E. Girot, K. Mozet, G. Medjahdi, R. Schneider, High performance Ce-doped ZnO nanorods for sunlight-driven photocatalysis, Beilstein J. Nanotechnol. 7 (2016) 1338–1349.
[29] S. Park, S. Kim, G.J. Sun, D.B. Byeon, S.K. Hyun, W.I. Lee, C. Lee, ZnO-core/ZnSe-shell nanowire UV photodetector, J. Alloys Compd. 658 (2016) 459–464.
[30] L. Xie, Z. Ai, M. Zhang, R. Sun, W. Zhao, Enhanced hydrogen evolution in the presence of plasmonic Au-photo-sensitized g-C_3N_4 with an extended absorption spectrum from 460 to 640 nm, PLoS One 11 (2016), e0161397.
[31] K. Shingange, Z.P. Tshabalala, O.M. Ntwaeaborwa, D.E. Motaung, G.H. Mhlongo, Highly selective NH_3 gas sensor based on Au loaded ZnO nanostructures prepared using microwave-assisted method, J. Colloid Interface Sci. 479 (2016) 127–138.
[32] Y.L. Luo, ZnO microrods photodeposited with Au@Ag nanoparticles: synthesis, characterization and application in SERS, Colloid J. 71 (2009) 223–232.